Deep-Ultraviolet Nonlinear Optical Crystals: Ba$_3$P$_3$O$_{10}$X (X = Cl, Br)

Peng Yu,[†] Li-Ming Wu,*[,†] Liu-Jiang Zhou,[†,‡] and Ling Chen*[,†]

[†]Key Laboratory of Optoelectronic Materials Chemistry and Physics, Fujian Institute of Research on the Structure of Matter, Chinese Academy of Sciences, Fuzhou, Fujian 350002, People's Republic of China

[‡]University of Chinese Academy of Sciences, Beijing 100039, People's Republic of China

Ⓢ *Supporting Information*

ABSTRACT: Deep-ultraviolet nonlinear optical (deep-UV NLO) crystals are of worldwide interest for the generation of coherent light with wavelength below 200 nm by the direct second-harmonic generation (SHG) output from solid-state lasers. The unprecedented deep-UV NLO phosphates representing their own structure types, Ba$_3$P$_3$O$_{10}$Cl (BPOC), Ba$_3$P$_3$O$_{10}$Br (BPOB), have been discovered, which display moderate powder SHG intensities in type I phase matchable behaviors with a short UV cutoff edge of 180 nm (measured by a single crystal, one of the shortest values among phosphates to date). Insightfully, the geometry and polarization of the C_1-P$_3$O$_{10}^{5-}$ building unit are affected by the crystal packing. DFT calculations and cutoff energy dependent SHG coefficient analyses reveal that the SHG origin is from the cooperation of asymmetric C_1-P$_3$O$_{10}^{5-}$ anion, Ba^{2+} cation, and Cl$^-$/Br$^-$ anion.
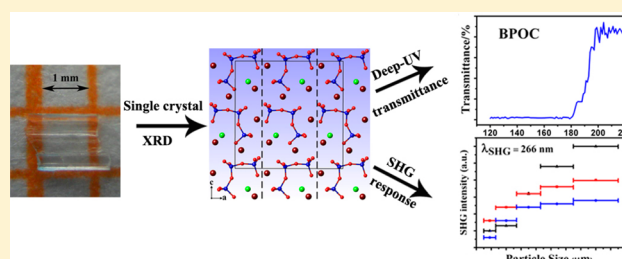
■ INTRODUCTION

Nonlinear optical (NLO) crystals are the key materials in solid state laser light frequency conversion techniques that have important applications in many fields, such as laser communication, laser medical treatment, and laser micromachining.[1−4] Usually, NLO materials are classified into three categories according to their working wavelength ranges in the spectrum: ultraviolet−visible (UV−vis),[1,2,5−10] infrared (IR),[11−14] and deep-ultraviolet (deep-UV, below 200 nm) materials.[15−19] The most advanced, commercially available benchmark NLO materials, β-BaB$_2$O$_4$ (BBO),[1] LiB$_3$O$_5$ (LBO),[2] KH$_2$PO$_4$ (KDP),[9] and KTiPO$_5$ (KTP),[10,20] belong to UV−vis materials. Yet, materials working in the other two regions are relatively rare. For example, commercial IR NLO benchmark materials including AgGaQ$_2$ (Q = S, Se)[12,21] and ZnGeP$_2$[13] suffer drawbacks of the low laser damage threshold or the two-photon absorption,[22] and several other newly discovered IR NLO compounds, such as Ba$_3$CsGa$_5$Se$_{10}$Cl$_2$,[11] La$_4$InSbS$_9$,[23] Sm$_4$GaSbS$_9$,[24] Ba$_{23}$Ga$_8$Sb$_2$S$_{38}$,[25] RbMn$_4$In$_5$Se$_{12}$,[26] and Cs$_2$HgI$_2$Cl$_2$[27] are in preliminary stage, whereas KBe$_2$BO$_3$F$_2$ (KBBF)[18,28] is the only practically usable deep-UV material to date that generates coherent light of wavelength below 200 nm by the direct second-harmonic generation (SHG).[16] Unfortunately, KBBF is very poisonous, according to the International Agency for Research on Cancer (IARC) that classified beryllium and beryllium compounds as Category 1 carcinogens.[29,30] Furthermore, KBBF crystal features a strong growth habit of layering because of the weak interlayer interactions, which makes it extremely difficult to grow into single crystals with large thickness; thus, the coherent light output power is severely limited.[16]

Deep-UV coherent light is in increasingly urgent demand in many important applications, for instance, semiconductor photolithography, laser micromachining, and modern scientific instruments.[18] However, exploration of deep-UV NLO materials is a great challenge because of the extremely rigorous prerequisite that includes not only the non-centrosymmetric crystallographic structure and considerable chemical stability, but also a rigorous wide band gap (wider than 6.0 eV in order to generate coherent light with wavelength below 200 nm). Consequently, the deep-UV NLO compound is severely limited within borates, beyond which no example is known to date. The recent examples include BPO$_4$,[31] Na$_2$CsBe$_6$B$_5$O$_{15}$,[19] NaBeB$_3$O$_6$,[32] NaSr$_3$Be$_3$B$_3$O$_9$F$_4$,[33] NaCaBe$_2$B$_2$O$_6$F,[34] Cs$_2$SiB$_4$O$_9$,[16] Ba$_4$B$_{11}$O$_{20}$F,[17] and K$_3$B$_6$O$_{10}$Cl.[35] Among them, the boron phosphate[31] and silicide and halide borates[16,17,35] are impressive with short deep-UV cutoff edges (130, 190, 175, and 180 nm) and high SHG intensities (2×, 4.6×, 10×, and 4× KDP). On the other hand, there are some known NLO active phosphates, but none of them are suitable working as a deep-UV material because of the inadequate absorption edge: for example, KTP (with absorption edge of 350 nm by single crystal),[10] KDP (with an theoretical absorption edge of 174 nm that is unfortunately unreachable because the unavoidable defects in the crystals that decrease considerably the band gap[10]), and Te$_2$O(PO$_4$)$_2$ (with absorption edge of 310 nm by polycrystalline sample).[10]

Here, we discover the first non-boron-containing deep-UV NLO phosphates with their own structure types, Ba$_3$P$_3$O$_{10}$Cl (BPOC) and Ba$_3$P$_3$O$_{10}$Br (BPOB), showing short deep-UV
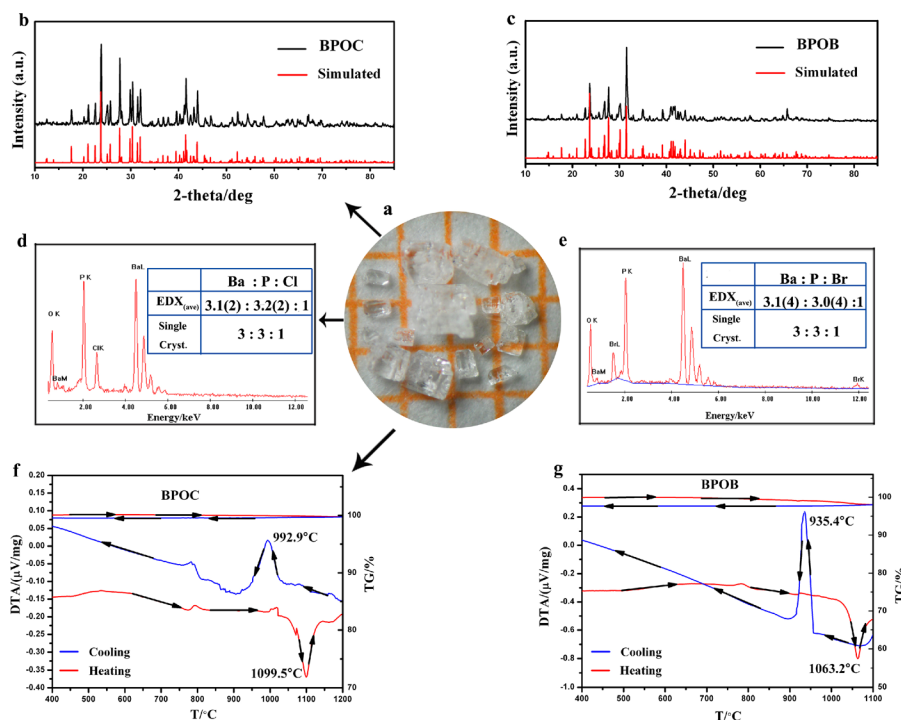
Figure 1. Photo of the as-synthesized BPOC crystals (a). Experimental and simulated X-ray powder diffraction patterns of BPOC (b) and BPOB (c). EDX results of BPOC (d) and BPOB (e). DTA and TG curves for BPOC (f) and BPOB (g).

cutoff edges, 180 nm by BPOC single crystal (one of the shortest values among phosphates to date) and <200 nm by polycrystalline BPOB. These compounds are type-I phase matchable with moderate powder SHG intensities (about 0.6× and 0.5× KDP), melt congruently, and exhibit wide transparent regions. Insightfully, the geometry and polarization of the C_1-$P_3O_{10}^{5-}$ building unit are affected by the different crystal packing. The SHG origin has also been discussed. These results highlight phosphate as a novel promising field for the future exploration of deep-UV NLO materials.

■ EXPERIMENTAL SECTION

Synthesis. BaO (99.5%, Alfa-Aesar), P_2O_5 (99.99%, Aladdin), BaCl$_2$ (99.95%, Alfa-Aesar), BaBr$_2$ (99.999%, Alfa-Aesar), CsCl (99.9%, Aladdin), and CsBr (99.9%, Aladdin) were used as received. All the manipulations were performed in an Ar-filled glovebox with controlled oxygen and moisture levels below 0.1 ppm. A total of 300 mg of BaO, P_2O_5, and BaCl$_2$ in the ratio of 5:3:1 was mixed with 300 mg of CsCl in a graphite crucible in the glovebox. Such a graphite crucible was sealed in evacuated fused-silicon tubes under 10^{-3} Pa, and then heated in a tube furnace from room temperature to 250 °C in 15 h, held for 24 h, then heated to 620 °C at a rate of 18.5 °C/h, and to 850 °C at 8 °C/h, following a hold time of 100 h, then subsequently cooled to 450 °C at 5 °C/h before the furnace was turned off. The excess flux was washed off by distilled water. BPOC was obtained as colorless block crystals (Figure 1a).

BPOB was synthesized with similar procedures. Both BPOC and BPOB are colorless and are stable in air at room temperature for several years. The phase purity has been confirmed by the powder X-ray diffraction patterns matching well with the simulated ones. (Figure 1b and c).

Large Crystal Growth. A mixture of as-synthesized polycrystalline BPOC (3.7 g) and CsCl (1.8 g) was loaded

into a platinum crucible, and sealed in an evacuated fused-silicon tube under 10^{-3} Pa. Such an assembly was placed in a muffle furnace, gradually heated to 800 °C, followed by a hold of 70 h, and then cooled to 450 °C at a rate of 0.5 °C/h before the furnace was turned off. Colorless and transparent crystals (Figure 2b) of 1.2 × 1.1 × 0.4 mm^3 were obtained. Unfortunately, a similar procedure only yielded tiny BPOB crystals with sizes less than a millimeter.

Crystal Structure Determinations. The single crystal X-ray diffraction data were collected on a Rigaku Mercury CCD diffractometer equipped with a graphite-monochromated Mo Kα radiation source (λ = 0.710 73 Å) at 293 K. The colorless single crystals were mounted on the tip of glass fibers for data collections. The data were corrected for Lorentz factors, polarization, and air absorption. Absorption corrections based on a multiscan technique were performed by the SADABS program.[36] All structures were solved by the direct methods and refined by full-matrix least-squares fitting on F^2 by SHELX-97.[37] All of the atoms were refined with anisotropic displacement parameters and secondary extinction correction. The space group was determined to be non-centrosymmetric space group $Pca2_1$ (NO. 29) for BPOC based on systematic absences, E-value statistics, and subsequent successful refinements with R_1 = 0.0357, wR_2 = 0.0469, and Flack parameter = 0.01(2). The BPOB was first refined in the space group $Pca2_1$, which generated unreasonably high R values of R_1 = 0.3506, wR_2 = 0.7425, and abnormal thermal parameters. Subsequently, BPOB was refined in the space group $P2_12_12_1$ and converged to considerably improved R_1 = 0.0329, wR_2 = 0.0708 with Flack parameter = 0.000(14). Crystallographic data and structural refinements for the compounds are summarized in Table 1; and the atomic positions, thermal parameters, and the selected bond distances are given in Tables 2, 3, and S1 and S2.

Powder X-ray Diffraction. The powder XRD patterns were collected using a Rigaku DMAX 2500 diffractometer with
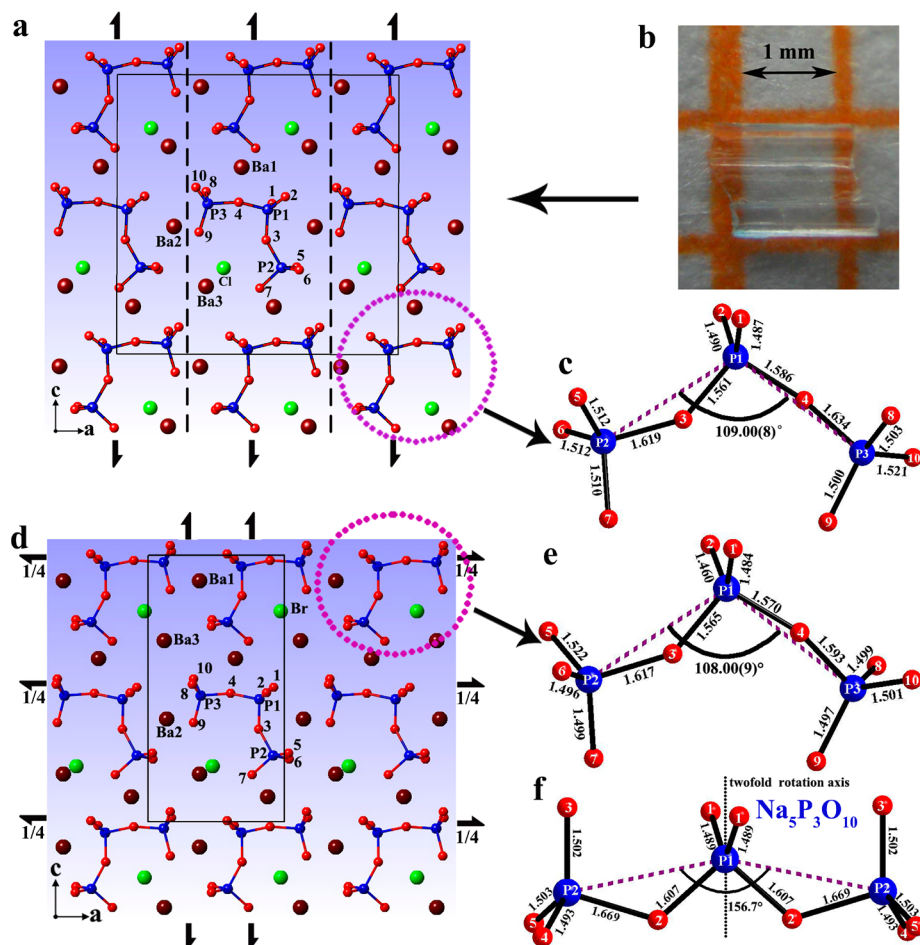
Figure 2. (010) views of structure of BPOC (a) and BPOB (d) with unit cell and atom number marked: dark red, Ba^{2+}; green, Cl^- or Br^-; red, O^{2-}; blue, P^{5+}. The positions of selected 2_1 screw axes and glide planes are indicated. (b) As-grown BPOC single crystal. The structures of triphosphate anions with atom number, P–O bond length and P–P–P angle marked: C_1-$P_3O_{10}^{5-}$ in BPOC (c) and BPOB (e), 2-$P_3O_{10}^{5-}$ in $Na_5P_3O_{10}$[48] (f).

Table 1. Crystal Data and Structure Refinements for BPOC and BPOB[a]

Compound	$Ba_3P_3O_{10}Cl$	$Ba_3P_3O_{10}Br$
Formula weight	700.35	744.8
Crystal system	Orthorhombic	Orthorhombic
Crystal color	colorless	colorless
Space group	$Pca2_1$ (NO. 29)	$P2_12_12_1$ (NO. 19)
a (Å)	14.2771(17)	7.1722(18)
b (Å)	5.5968(4)	11.364(3)
c (Å)	14.1592(13)	13.998(4)
$\alpha = \beta = \gamma$ (deg.)	90	90
V (Å^3)	1131.41(19)	1140.9(5)
Z	4	4
D_c (g.cm^{-3})	4.193	4.336
μ (mm^{-1})	11.024	14.201
GOOF on F^2	1.151	1.086
Flack parameter	0.01(2)	0.000(14)
R_1, wR_2 ($I > 2\sigma(I)$)[a]	0.0289, 0.0443	0.0328, 0.0707
R_1, wR_2 (all data)	0.0357, 0.0469	0.0329, 0.0708
Largest diff peak/hole, e Å^{-3}	0.75/−0.87	2.88/−3.32

[a]$R1 = \sum \|F_o|-|F_c\| / \sum |F_o|$ for $F_o^2 > 2\sigma(F_o^2)$; $wR2 = \sum [w\ (F_o^2-F_c^2)] / \sum [w(F_o^2)^2]^{1/2}$, where $w = 1/[\sigma^2 F_o^2 + (AP)^2 + BP]$, and $P = (F_o^2 + 2F_c^2)/3$.

monochromatized Cu–Kα radiation at room temperature in the 2θ range of 10−85° with a scan step width of 0.05°. The

measured X-ray powder diffraction patterns were in accordance with the calculated ones simulated from the single crystal data as shown in Figures 1b and 1c.

Elemental Analysis. Semiquantitative microprobe analyses on the compounds were performed with the aid of a field emission scanning electron microscope (Nova NanoSEM 230) equipped with an energy dispersive X-ray spectroscope (EDX). The energy dispersive spectra taken on visibly clean surfaces of the sample proved the presence of Ba, P, and Cl/Br in the ratios of $Ba_{3.1(2)}P_{3.2(2)}Cl$ and $Ba_{3.1(4)}P_{3.0(4)}Br$ (Figure 1d and e, Tables S3 and S4).

UV−vis−NIR Diffuse Reflectance and Infrared Spectra. The UV−vis−NIR transmittance spectra were measured on the polycrystalline samples of BPOC and BPOB by a Perkin-Elmer Lambda 900 UV−vis−NIR spectrometer equipped with an integrating sphere over a 190−2500 nm wavelength range at room temperature and a $BaSO_4$ plate as a reference, on which the finely ground sample powders were coated. The IR spectra were measured by using a Nicolet Magana 750 FT−IR spectrophotometer in the range of 2.5−25 μm and a total of 100 mg of polycrystalline samples (BPOC or BPOB) and KBr in the ratio of 100:1 were ground and pressed into transparent pellets, which suggest the existence of $P_3O_{10}^{5-}$ anions in the structures of BPOC and BPOB.

Deep-UV Transmittance Spectrum. The deep-UV optical transmittance spectrum was measured on a BPOC

Table 2. Atomic Coordinates and Equivalent Isotropic Displacement Parameters of BPOC

Atom	Oxidation	Wyckoff	occ.	x	y	z	U (eq)
Ba1	+2	4a	1.00	0.44232(3)	0.01266(7)	0.66992(2)	0.01050(11)
Ba2	+2	4a	1.00	0.70271(3)	0.00268(9)	0.45672(3)	0.01086(10)
Ba3	+2	4a	1.00	0.68288(3)	0.50089(9)	0.74300(3)	0.01181(11)
Cl	−1	4a	1.00	0.62058(16)	0.0037(4)	0.80874(18)	0.0238(4)
P1	+5	4a	1.00	0.53485(14)	0.4966(3)	0.51840(14)	0.0096(4)
P2	+5	4a	1.00	0.58515(13)	0.4863(4)	0.31048(12)	0.0097(4)
P3	+5	4a	1.00	0.32257(13)	0.4913(4)	0.53826(12)	0.0088(4)
O1	−2	4a	1.00	0.5508(4)	0.7534(9)	0.5400(5)	0.0175(13)
O2	−2	4a	1.00	0.5980(4)	0.3202(10)	0.5649(4)	0.0200(14)
O3	−2	4a	1.00	0.5298(5)	0.4553(12)	0.4095(4)	0.0306(17)
O4	−2	4a	1.00	0.4323(3)	0.4100(9)	0.5445(4)	0.0121(12)
O5	−2	4a	1.00	0.6385(4)	0.7196(8)	0.3128(4)	0.0134(12)
O6	−2	4a	1.00	0.6481(4)	0.2699(8)	0.3028(4)	0.0130(12)
O7	−2	4a	1.00	0.5082(3)	0.4817(9)	0.2373(4)	0.0143(11)
O8	−2	4a	1.00	0.3159(4)	0.7352(11)	0.5821(4)	0.0163(14)
O9	−2	4a	1.00	0.2919(4)	0.4827(10)	0.4370(3)	0.0169(12)
O10	−2	4a	1.00	0.2796(4)	0.2921(9)	0.5971(4)	0.0147(13)

$^{a}U_{eq}$ is defined as one-third of the trace of the orthogonalized U_{ij} tensor.

Table 3. Selected Bond Lengths (Å) of BPOC

$Ba_3ClP_3O_{10}$			
Ba1−O1	2.809(6)	Ba3−O7	2.731(5)
Ba1−O2	3.180(6)	Ba3−O8	3.247(6)
Ba1−O4	2.849(5)	Ba3−O9	2.772(5)
Ba1−O5	2.770(6)	Ba3−O10	2.742(6)
Ba1−O6	2.776(6)	Ba1−Cl	3.216(2)
Ba1−O7	3.011(5)	Ba2−Cl	3.279(2)
Ba1−O7	3.068(5)	Ba3−Cl	2.997(6)
Ba1−O8	2.686(6)	Ba3−Cl	3.066(2)
Ba1−O10	2.985(6)	P1−O1(T)	1.487(5)
Ba2−O1	2.836(5)	P1−O2(T)	1.490(6)
Ba2−O2	2.782(6)	P1−O3(B)	1.561 (6)
Ba2−O5	2.739(6)	P1−O4(B)	1.585 (5)
Ba2−O6	2.756(6)	P2−O3(B)	1.619 (6)
Ba2−O8	2.813(6)	P2−O5(T)	1.512(5)
Ba2−O9	3.013(6)	P2−O6(T)	1.512(5)
Ba2−O9	3.162(6)	P2−O7(T)	1.512(5)
Ba2−O10	2.806(6)	P3−O4(B)	1.634(5)
Ba3−O2	2.975(6)	P3−O8(T)	1.503(6)
Ba3−O5	2.997(6)	P3−O9(T)	1.499(5)
Ba3−O6	2.866(5)	P3−O10(T)	1.521(6)

T: Terminal $O^{2−}$ anion. B: Bridging $O^{2−}$ anion.

single crystal of size $1.2 \times 1.1 \times 0.4$ mm³ at room temperature using a spectrophotometer (VUVas2000, McPherson) in the wavelength range of 120−380 nm.

Second Harmonic Generation Measurements. Powder SHG were measured on the polycrystalline samples of BPOC and BPOB by using the Kurtz and Perry method with Q-switched Nd:YAG lasers at the wavelength of 1064 nm and its SHG at 532 nm.[38] The SHG intensity depended strongly on the particle size of the sample, and thus, polycrystalline samples were ground and sieved into a series of distinct size ranges of 30−46, 46−74, 74−106, 106−150, and 150−210 μm, respectively, which were pressed between glass slides and secured with tape in 1-mm-thick aluminum holders containing a hole with diameter of 8 mm, and the powdered commercial KDP sample sieved into the same size range was used as the reference.

Thermal Analyses. Different thermal analysis (DTA) and thermogravimetric analysis (TG) of BPOC and BPOB were carried out on a NETZSCH STA 449C simultaneous analyzer. The sample was enclosed in an Al_2O_3 crucible, heated at a rate of 30 °C/min from room temperature to 1100 °C, and then cooled to room temperature at a rate of 30 °C/min under flowing nitrogen.

Calculations of Electronic Structures and Optical Properties. Electronic structures of BPOC and BPOB were calculated based on the density functional theory (DFT),[39] with the aid of Vienna ab initio simulation package (VASP). The generalized gradient approximation (GGA)[40] was chosen as the exchange-correlation functional, and a plane-wave basis with projector augmented wave (PAW) potentials[41] was used. The plane-wave cutoff energy of 400 eV and threshold of 10^{-5} eV were set for the self-consistent-field convergence of the total energy. The interactions between ionic core and electron were described by the norm-conserving pseudopotential. Ba $5s^25p^66s^2$, P $3s^23p^3$, O $2s^22p^4$, Br $4s^24p^5$, and Cl $3s^23p^5$ were treated as valence electrons. The k integration over the Brillouin zone was performed by the tetrahedron method. A k-point spacing with 0.02 Å^{-1} (i.e., $7 \times 7 \times 7$ k-point grid) in the Brillouin zone was used for BPOC, BPOB, and KDP. The same k-point grids were used in the optical property calculations.

The static and dynamic second-order nonlinear susceptibility $\chi^{abc}(-2\omega,\omega,\omega)$ were calculated based on the so-called length-gauge formalism by Aversa and Sipe.[42,43] According to the d_{ave}−E_g curves (Figure S4a and b), the band gaps were predicted to be 7.64 and 6.49 eV for BPOC and BPOB, which are comparable with the experimental values. (6.89 and >6.22 eV) Consequently, scissor values of 2.06 eV for BPOC and 1.23 eV for BPOB were applied respectively in the subsequent optical properties calculations.

More than 500 empty bands were used in the optical property calculations. The linear optical properties in terms of the complex dielectric function $\varepsilon(\omega) = \varepsilon_1(\omega) + i\varepsilon_2(\omega)$ were calculated,[44,45] and optical constants were obtained from the imaginary part of the dielectric function $\varepsilon_2(\omega)$ via the Kramers-Kroning transform.[46,47]
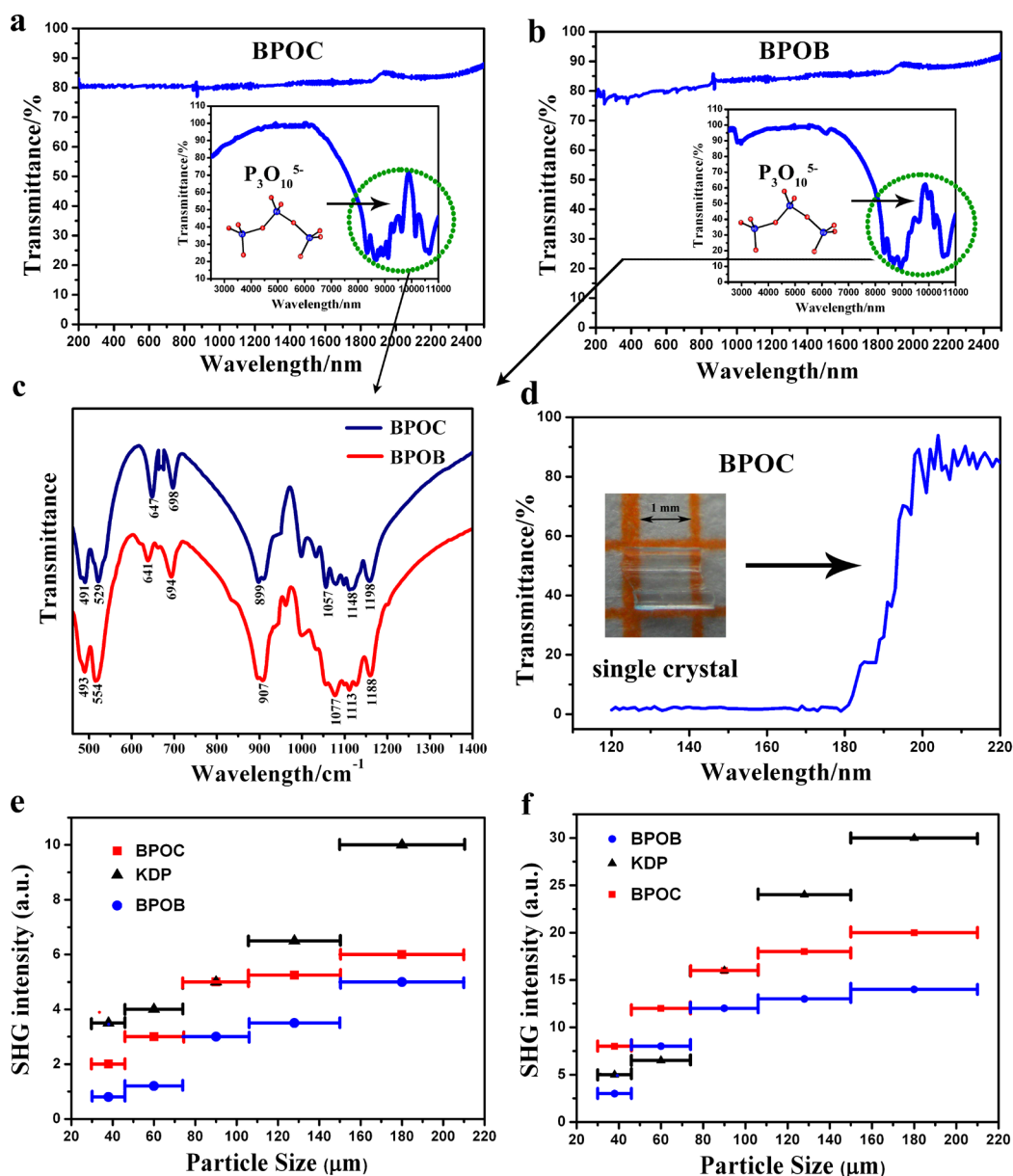
Figure 3. Transmittance of the polycrystalline samples of BPOC (a) and BPOC (b) in UV−vis−IR and IR (inset panel) regions. (c) IR spectra of BPOC (navy curve) and BPOB (red curve). (d) Transmittance of a BPOC single crystal in the deep UV and UV region. Phase-matching curves, i.e., particle size vs SHG intensity, of polycrystalline BPOC and BPOB at the wavelengths of 1064 nm (e) and 532 nm (f); KDP is used as a reference.

RESULTS AND DISCUSSION

Crystal Structure. BPOC crystallizes in the acentric orthorhombic space group $Pca2_1$ with a novel structure type (Figure 2a,b, and Table 1). Instead of being isostructural to BPOC, BPOB crystallizes in the polar orthorhombic space group $P2_12_12_1$ with its own structure type (Figure 2d, Table 1). Both BPOC and BPOB are constructed of novel asymmetric isolated $P_3O_{10}^{5-}$ anionic building units (Figure 2c,e). Such discrete anions show no symmetry operation except C_1 (denoting as C_1-$P_3O_{10}^{5-}$ hereafter), which differ from the known 2-$P_3O_{10}^{5-}$ anion (showing a twofold rotation axis symmetry) in the NLO inert compound $Na_5P_3O_{10}$[48] (Figure 2f). Importantly, we realized that the crystal packing influence the bending and folding of such a C_1-$P_3O_{10}^{5-}$ anion that gives rise to the NLO property as discussed below. As illustrated in Figure 2c,e vs f, the P−P−P angles can vary from 156.7° in $Na_5P_3O_{10}$[49] to 109.00(8)° in BPOC or 108.00(9)° in BOPB.

Each PO_4 tetrahedron in BPOC and BPOB is slightly distorted with O−P−O angles ranging from 93.9(5)° to 117.2(4)°, and P−O bonds ranging from 1.460(12) to 1.634(5) Å. Such distortions result in the asymmetric local coordination without any mirror plane symmetry in C_1-$P_3O_{10}^{5-}$ anions (Tables 2, S2). Despite the distortion, the P−O bonds are still comparable to both the sum of the Shannon crystal radii of P^{5+} (0.31 Å) and O^{2-} (1.24 Å) and those in P_4O_{10} (1.39−1.62 Å),[49] $(NH_4)_4P_4O_{12}$ (1.46−1.61 Å),[50] and $Na_5P_3O_{10}$ (1.50−1.68 Å).[48] Data in Table 2 indicate that the P−O$_{(terminal)}$ bonds (namely, O1, O2, O5−10) (1.487(5)−1.521(6) Å) are shorter than the P−O$_{(bridging)}$ bonds (O3, O4) (1.561(6)−1.634(5) Å). Obviously, in comparison with $Na_5P_3O_{10}$,[48] the different crystal packings of BPOC and BPOB cause the distortions of C_1-$P_3O_{10}^{5-}$ building units (Figure S2). As shown in Figure 2a, looking down the b axis of BPOC, the C_1-$P_3O_{10}^{5-}$ building unit generates itself through the 2_1-screw axis at (0, 0, 1/2) along
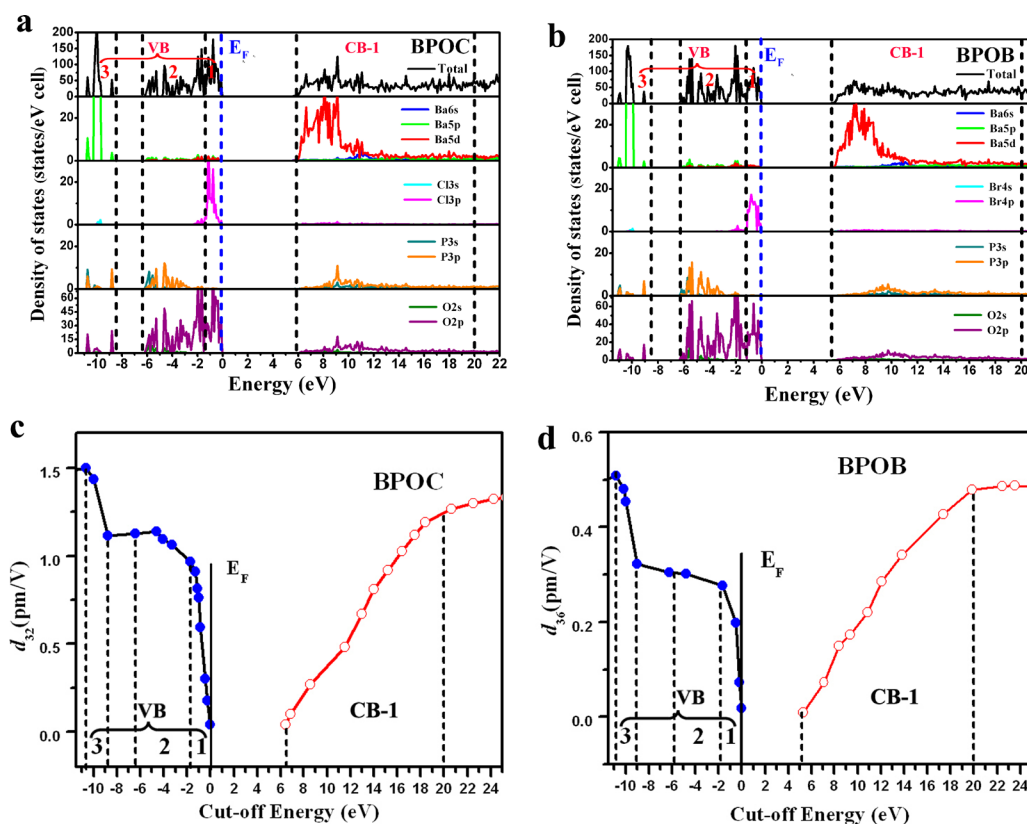
Figure 4. Total and partial densities of states of BPOC (a) and BPOB (b); numbers represent different band regions. Cutoff-energy-dependent static SHG coefficient of BPOC (c) and BPOB (d).

the c axis, and operates itself by the c-glide plane $(1/4, y, z)$, and eventually crystallizes in the $Pca2_1$ symmetry. Differently, the (010) view of BPOB reveals that the C_1-$P_3O_{10}^{5-}$ units are related only by 2_1-screw axes, such as $1/4, 0, z; x, 1/4, 0$ (Figure 2d). The different packings of BPOC and BPOB are the direct result of the size difference between Cl^- and Br^- anions, which first leads to the different Ba2-polyhedra, i.e., the ninefold coordinated $Ba2O_8Cl$ polyhedron in BPOC vs the eightfold coordinated $Ba2O_7Br$ in BPOB (Figure S1). Each compound contains Ba1-polyhedron (tenfold coordinated $Ba1O_9X$) and Ba3-polyhedron (ninefold coordinated $Ba3O_7X_2$) whose geometries are in principle the same except for the obvious different Ba–X bond length (Ba–Cl: 2.997(6)–3.279(2) Å vs Ba–Br: 3.1706(16)–3.4602(16) Å) (Figure S1; and Tables 2 and S2) The Ba–O distances ranging from 2.686(6) to 3.247(6) Å are comparable with those in $BaIn_2P_4O_{14}$ (2.809(3) to 3.124(3) Å).[51] In short, the bending and folding flexibility of the $P_3O_{10}^{5-}$ unit is clear (also confirmed by the IR vibration spectra discussed below), and it is affected by the different crystal packing, which eventually lead to the formation of the NLO active title compounds or the formation of the NLO inert $Na_5P_3O_{10}$.[48]

Thermal Stability. As shown in Figure 1f and g, the differential thermal (DTA) and thermogravimetric (TG) curves of the polycrystalline BPOC and BPOB reveal no weight loss from room temperature to 1200 °C. Melting endothermic absorption peaks at 1099.5 and 1063.2 °C on the heating run, as well as the crystallization exothermic peaks at 992.9 and 935.4 °C on the cooling run, are observed for BPOB and BPOC, respectively. The powder XRD patterns of the residual samples after the thermal measurement revealed neither

decomposition nor phase transition. Multiple heating/cooling DTA cycles combined with TG were monitored on both BPOC and BPOB, confirming their good thermal stability with well-defined melting and crystallization points. These primary results suggest that large crystals of the title compounds should be grown easily.

Optical Properties. As presented in Figure 3a and b, the transmittance of BPOC and BPOB reveal wide transparencies from the UV−vis to middle IR region of the spectrum (180 nm to 8.31 μm for BPOC and <200 nm to 8.34 μm for BPOB, respectively). Two IR vibration characteristic bands of $P_3O_{10}^{5-}$ anion are observed in the range of 1057−1198 cm^{-1} and 899 cm^{-1} for BPOC, and 1077−1188 cm^{-1} and 907 cm^{-1} for BPOB, which are in accordance with those in $Na_5P_3O_{10}$ (1100−1200 cm^{-1} and 900 cm^{-1})[52] (Figure 3c). The characteristic bands (1057−1198 cm^{-1} for BPOC, 1077−1188 cm^{-1} for BPOB) are attributed to the P−O asymmetrical stretching vibrations, whereas the 899 and 907 cm^{-1} bands belong to the symmetrical $P_3O_{10}^{5-}$ stretching vibrations, which match well with the reported values.[53] The slight deviations in the absorption peak position and shape confirm the structural bending and folding of $P_3O_{10}^{5-}$ anions in BPOC, BPOB in comparison with those of $Na_5P_3O_{10}$.[54] Since BPOC and BPOB do not show any obvious absorption peak down to 200 nm according to the UV−vis transmittance spectra (Figure 3a,b), it can be deduced that their band gaps should be wider than 6.22 eV. Fortunately, we obtained a single BPOC crystal of $1.2 \times 1.1 \times 0.4$ mm^3 in size (Figure 2b), large enough to measure the single crystal deep-UV optical transmittance spectrum. Remarkably, the UV short-wavelength absorption edge is located at about 180 nm (Figure 3d). This suggests a band

gap of 6.89 eV that agrees well with both the color and the theoretical evaluation discussed below. Such an absorption edge is one of the shortest values among phosphates to date, such as KTP (350 nm by single crystal),[10] $Te_2O(PO_4)_2$ (310 nm by polycrystalline sample),[10] and it is close to the unreachable ideal absorption edge (because of the unavoidable defects that decrease the band gap considerably) of KDP (174 nm).[10] Markedly, such a deep-UV absorption edge is comparable to those of some borates, such as the only usable deep-UV material KBBF (155 nm by single crystal),[15] and BPO_4 (130 nm),[31] $Cs_2SiB_4O_9$[16] (below 190 nm by polycrystalline sample).

The powder SHG intensities of BPOC, BPOB, and KDP as reference were measured at 1064 and 532 nm light source by the Kurtz and Perry method.[38] As shown in Figure 3e and f, both BPOC and BPOB are type-I phase-matchable in both visible and UV regions, with SHG intensities about 0.6 and 0.5 times that of KDP. The relative SHG intensities in the UV region do not differ significantly from those in the visible region, and these intensities are comparable to those of KBBF ($(2.1-2.6) \times$ KDP)[15] and $Cs_2SiB_4O_9$ ($4.6 \times$ KDP).[16]

Theoretical Calculations. As shown in the energy band structures (Figure S3 and Table S5), BPOC has a direct band gap of 5.43 eV, and BPOB, an indirect band gap of 5.26 eV. These calculated values are in principle consistent with the experimental observations (6.89 eV for BPOC and >6.22 eV for BPOB). The obvious DFT underestimation of band gap is associated with the insufficient description of the eigenvalues of the electronic states for GGA, especially for insulates.[54,55] The total and projected densities of states (TDOS, PDOS) analyses shown in Figure 4 indicate that the valence bands (VB) lower than −8.5 eV (VB-3) mostly consist of Ba 5p, O 2p, and P 3p states. Strong P−O hybridizations occur in the energy range of −11 to −3 eV. The VB-2 region is predominately derived from O 2p states mixing with minor P 3p and P 3s states, and VB-1 is mainly composed of Br 4p/Cl 3p and O 2p states. The conductive band (CB) originates mainly from Ba 5d states, mixing with small amounts of P 3p, Ba 6s, and O 2p states. As a result, the optical absorptions can be assigned mainly to the electron transition from the p states of Br/Cl and O atoms to Ba 5d states. The PDOS of Ba 6s states almost locate above E_F, which means that the Ba atom acts primarily as an electron donor. Similarly, Cl and Br atoms act as electron acceptors because their p states are localized below E_F.

The interband electronic transitions between the occupied and unoccupied states are described by the imaginary part ε_2 (Figure S5), which indicates that the calculated basic absorption edges are 7.7 and 6.55 eV for BPOC and BPOB, respectively, in good comparison with the experimental values (6.89 and >6.22 eV). The absorption edges are mainly assigned to the interband electron transitions from O 2p and Cl 3p/Br 4p states to Ba 5d state. The average values of the polarized zero-frequency dielectric constants ε_1^{ave} (0) are calculated to be 2.38 and 2.64 for BPOC and BPOB (Figure S6). The energy dependent refractive index curves reveal that the static refractive indexes are 1.54, 1.56, and 1.53 for BPOC, and 1.62, 1.64, and 1.62 for BPOB, respectively. (Figure S7) These data are comparable with those of LBO. The birefringences (Δn) for BPOC/BPOB (Figure S8) are calculated to be 0.028/ 0.023 at the wavelength of 1064 nm (1.17 eV) which are comparable with that of LBO ($0.040_{(exp)}$, phase-matchable) and agree well with the experimental phase matchability in the visible region (Figure 3e). The Δn for BPOC/BPOB are calculated to be 0.030/0.024 at 532 nm (2.33 eV); yet, these compounds are phase matchable in the UV region as shown in Figure 3f. We thus consider the theoretical calculated birefringence values may be underestimated. The reflectivity $R(\omega)$ (Figure S9) is less than 5% in the deep UV to visible regions, which suggests a very good photopermeability, confirmed by the calculated absorption coefficient curves (Figure S10).

The dynamic SHG coefficients of BPOC, BPOB, and KDP are studied (Figure S11). At the wavelength of 1064 nm (i.e., 1.17 eV), the $d_{ave} = ((2d_{15} + 2d_{24} + d_{33})/5)$ is calculated to be 0.57 and 0.49 pm/V for BPOC and BPOB, slightly smaller than the $d_{36} = 0.96$ pm/V of KDP, which in principle agrees with the experimental observation. The source of the SHG response has been investigated via the cutoff-energy-dependent SHG coefficient[6,56] according to the length-gauge formalism.[42,43] As shown in Figure 4c and d, the SHG response originates dominantly from VB-1, VB-3, and CB-1 regions. As discussed above, the VB-1 is predominately derived from the filled O 2p and Cl 3p/Br 4p states, and VB-3 is mainly derived from the filled Ba 5p, O 2p, and P 3p states, whereas CB-1 is mostly unoccupied Ba 5d state and unoccupied P−O states. Thus, the SHG response may originate from the electron transition from the occupied O 2p, Cl 3p/Br 4p, Ba 5p, and P 3p states to the unoccupied Ba 5d and unoccupied P 3p and O 2p states. Consequently, the cooperation of C_1-$P_3O_{10}^{5-}$ anions, Ba^{2+} cation, and Cl^-/Br^- halide anions is responsible for the SHG response.

■ CONCLUSION

In summary, the first non-boron-containing deep-UV NLO active phosphates with their own structure types, $Ba_3P_3O_{10}Cl$ (BPOC) and $Ba_3P_3O_{10}Br$ (BPOB), have been discovered by high-temperature solid-state reactions. The single crystal structures are constructed by isolated asymmetric C_1-$P_3O_{10}^{5-}$ building units, Ba^{2+} cations, and Cl^-/Br^- anions. Interestingly, the different crystal packing of the discrete $P_3O_{10}^{5-}$ building unit affects its bending and folding geometry and results in its asymmetry, which leads to the NLO property of the compound. These congruently melting compounds have moderate powder SHG intensities in type-I phase matchable behaviors with intensities about 0.6, 0.5 times that of benchmark KH_2PO_4 (KDP). Remarkably, BPOC single crystal exhibits a UV cutoff edge of 180 nm, which is one of the shortest values among phosphates to date. Theoretical studies reveal that the SHG response originates from the cooperation of C_1-$P_3O_{10}^{5-}$ anion, Ba^{2+} cation, and Cl^-/Br^- anion. Because of the structural flexibility of the $P_3O_{10}^{5-}$ building units, by adjusting its crystal-packing pattern, more non-centrosymmetric compounds are anticipated. The discoveries in this article would open up a novel pathway for finding and designing new NLO materials.

■ ASSOCIATED CONTENT

ⓢ Supporting Information
The cif file, additional tables and figures. This material is available free of charge via the Internet at http://pubs.acs.org.

■ AUTHOR INFORMATION

Corresponding Authors
*E-mail: chenl@fjirsm.ac.cn.
*E-mail: liming_wu@fjirsm.ac.cn.

Notes

The authors declare no competing financial interest.

■ REFERENCES

(1) Chen, C. T.; Wu, B. C.; Jiang, A. D.; You, G. M. *Sci. Sin., Ser. B (Engl. Ed.)* **1985**, *28*, 235.

(2) Chen, C. T.; Wu, Y. C.; Jiang, A. D.; Wu, B. C.; You, G. M.; Li, R. K.; Lin, S. J. *J. Opt. Soc. Am. B* **1989**, *6*, 616.

(3) Burland, D. M. *Chem. Rev.* **1994**, *94*, 1.

(4) Ok, K. M.; Chi, E. O.; Halasyamani, P. S. *Chem. Soc. Rev.* **2006**, *35*, 710.

(5) (a) Reshak, A. H.; Auluck, S.; Kityk, I. V. *Phys. Rev. B* **2007**, *75*, 245120. (b) Reshak, A. H.; Chen, X. A.; Auluck, S.; Kityk, I. V. *J. Chem. Phys.* **2008**, *129*, 204111.

(6) Huang, Y. Z.; Wu, L. M.; Wu, X. T.; Li, L. H.; Chen, L.; Zhang, Y. F. *J. Am. Chem. Soc.* **2010**, *132*, 12788.

(7) Chen, C. T.; Lu, J. H.; Wang, G. L.; Xu, Z. Y.; Wang, J. Y.; Zhang, C. Q.; Liu, Y. G. *Chin. Phys. Lett.* **2001**, *18*, 1081.

(8) Ra, H. S.; Ok, K. M.; Halasyamani, P. S. *J. Am. Chem. Soc.* **2003**, *125*, 7764.

(9) De Yoreo, J. J.; Burnham, A. K.; Whitman, P. K. *Int. Mater. Rev.* **2002**, *47*, 113.

(10) Dimitriev, V. G. *Handbook of Nonlinear Optical Crystals*; Springer: Berlin, 1991.

(11) Yu, P.; Zhou, L. J.; Chen, L. *J. Am. Chem. Soc.* **2012**, *134*, 2227.

(12) Boyd, G. D.; Kasper, H.; Mcfee, J. H. *IEEE. J. Quantum Elect.* **1971**, *7*, 563.

(13) Boyd, G. D.; Buehler, E.; Storz, F. G. *Appl. Phys. Lett.* **1971**, *18*, 301.

(14) Chung, I.; Jang, J. I.; Malliakas, C. D.; Ketterson, J. B.; Kanatzidis, M. G. *J. Am. Chem. Soc.* **2010**, *132*, 384.

(15) Chen, C. T.; Wang, Y. B.; Wu, B. C.; Wu, K. C.; Zeng, W. L.; Yu, L. H. *Nature* **1995**, *373*, 322.

(16) Wu, H. P.; Yu, H. W.; Pan, S. L.; Huang, Z. J.; Yang, Z. H.; Su, X.; Poeppelmeier, K. R. *Angew. Chem., Int. Ed.* **2013**, *52*, 3406.

(17) Wu, H. P.; Yu, H. W.; Yang, Z. H.; Hou, X. L.; Su, X.; Pan, S. L.; Poeppelmeier, K. R.; Rondinelli, J. M. *J. Am. Chem. Soc.* **2013**, *135*, 4215.

(18) Chen, C. T.; Wang, G. L.; Wang, X. Y.; Xu, Z. Y. *Appl. Phys. B* **2009**, *97*, 9.

(19) Wang, S. C.; Ye, N. *J. Am. Chem. Soc.* **2011**, *133*, 11458.

(20) Reshak, A. H.; Kityk, I. V.; Auluck, S. *J. Phys. Chem. B* **2010**, *114*, 16705.

(21) Reshak, A. H. *J. Phys.: Condens. Matter* **2005**, *369*, 243.

(22) Schunemann, P. G. *AIP Conf. Proc.* **2007**, *916*, 541.

(23) Zhao, H. J.; Zhang, Y. F.; Chen, L. *J. Am. Chem. Soc.* **2012**, *134*, 1993.

(24) Chen, M. C.; Li, L. H.; Chen, Y. B.; Chen, L. *J. Am. Chem. Soc.* **2011**, *133*, 4617.

(25) Chen, M. C.; Wu, L. M.; Lin, H.; Zhou, L. J.; Chen, L. *J. Am. Chem. Soc.* **2012**, *134*, 6058.

(26) Lin, H.; Chen, L.; Zhou, L. J.; Wu, L. M. *J. Am. Chem. Soc.* **2013**, *135*, 12914.

(27) Zhang, G.; Li, Y. J.; Jiang, K.; Zeng, H. Y.; Liu, T.; Chen, X. G.; Qin, J. G.; Lin, Z. S.; Fu, P. Z.; Wu, Y. C.; Chen, C. T. *J. Am. Chem. Soc.* **2012**, *134*, 14818.

(28) Wu, B. C.; Tang, D. Y.; Ye, N.; Chen, C. T. *Opt. Mater.* **1996**, *5*, 105.

(29) IARC Monograph, Volume *58*. *International Agency for Research on Cancer*. 1993. Retrieved 2008−09−18.

(30) Puchta, R. *Nat. Chem.* **2011**, *3*, 416.

(31) (a) Schulze, G. E. R. *Zeitschrift fuer Physikalische Chemie, Abteilung B: Chemie der Elementarprozesse, Aufbau der Materie* **1934**, *24*, 215−240. (b) Li, Z. H.; Lin, Z. H.; Wu, Y. C.; Fu, P. Z.; Wang, Z. Z.; Chen, C. T. *Chem. Mater.* **2004**, *16*, 2906. (c) Xu, G. G.; Li, J.; Han, S. J.; Guo, Y. J.; Wang, J. Y. *Crystallogr. Rep.* **2010**, *55*, 1242. (d) Zhao, S. G.; Zhang, G. C.; Feng, K.; Lu, J.; Wu, Y. C. *Cryst. Res. Technol.* **2012**, *47*, 391−396.

(32) Wang, S. C.; Ye, N.; Li, W.; Zhao, D. *J. Am. Chem. Soc.* **2010**, *132*, 8779.

(33) Huang, H. W.; Yao, J. Y.; Lin, Z. S.; Wang, X. Y.; He, R.; Yao, W. J.; Zhai, N. X.; Chen, C. T. *Angew. Chem., Int. Ed.* **2011**, *50*, 9141.

(34) Huang, H. W.; Yao, J. Y.; Lin, Z.; Wang, X. Y.; He, R.; Yao, W. J.; Zhai, N. X.; Chen, C. T. *Chem. Mater.* **2011**, *23*, 5457.

(35) Wu, H. P.; Pan, S. L.; Poeppelmeier, K. R.; Li, H. Y.; Jia, D. Z.; Chen, Z. H.; Fan, X. Y.; Yang, Y.; Rondinelli, J. M.; Luo, H. S. *J. Am. Chem. Soc.* **2011**, *133*, 7786−7790.

(36) *CrystalClear*, v 1.3.5; Rigaku Corp., The Woodlands: TX, 1999.

(37) Sheldrick, G. M. *SHELXTL*, v 5.1; Bruker-AXS, Madison, WI, 1998.

(38) Kurtz, S. K.; Perry, T. T. *J. Appl. Phys.* **1968**, *39*, 3798.

(39) Kresse, G.; Furthmuller, J. *Phys. Rev. B* **1996**, *54*, 11169.

(40) Perdew, J. P.; Wang, Y. *Phys. Rev. B* **1992**, *45*, 13244.

(41) Kresse, G.; Joubert, D. *Phys. Rev. B* **1999**, *59*, 1758.

(42) Aversa, C.; Sipe, J. E. *Phys. Rev. B* **1995**, *52*, 14636.

(43) Rashkeev, S. N.; Lambrecht, W. R. L.; Segall, B. *Phys. Rev. B* **1998**, *57*, 3905.

(44) Okoye, C. M. I. *J. Phys., Condens. Matter* **2003**, *15*, 5945.

(45) Terki, R.; Bertrand, G.; Aourag, H. *Microelectron. Eng.* **2005**, *81*, 514.

(46) Laksari, S.; Chahed, A.; Abbouni, N.; Benhelal, O.; Abbar, B. *Comput. Mater. Sci.* **2006**, *38*, 223.

(47) Mo, S. D.; Ching, W. Y. *Phys. Rev. B* **1995**, *51*, 13023.

(48) Davies, D. R.; Corbridge, D. E. C. *Acta Crystallogr.* **1958**, *11*, 315.

(49) Cruickshank, D. W. J. *Acta Crystallogr.* **1964**, *17*, 677.

(50) Cruickshank, D. W. J. *Acta Crystallogr.* **1964**, *17*, 675.

(51) Zhang, W. L.; Chai, G. L.; Zhang, H.; Lin, C. S.; He, C. Z.; Cheng, W. D. *Mater. Res. Bull.* **2010**, *45*, 1796.

(52) Kijkowska, R.; Kowalski, Z.; Pawlowska-Kozinska, D.; Wzorek, Z. *Ind. Eng. Chem. Res.* **2004**, *43*, 5221.

(53) Popova, V. I.; Popov, V. A.; Sokolova, E. V.; Ferraris, G.; Chukanov, N. V. *Neues Jahrb. Mineral., Monatsh.* **2002**, 117.

(54) Etheredge, K. M. S.; Mackay, R.; Schimek, G. L.; Hwu, S. J. *Inorg. Chem.* **1996**, *35*, 7919.

(55) Godby, R. W.; Schluter, M.; Sham, L. J. *Phys. Rev. B* **1987**, *36*, 6497.

(56) Lee, M. H.; Yang, C. H.; Jan, J. H. *Phys. Rev. B* **2004**, *70*, 235110.